Kinetic mix at gas-shell interface in inverted corona fusion targets

W. M. Riedel, N. B. Meezan, D. P. Higginson, et al.

View Online   Export Citation   CrossMark

ARTICLES YOU MAY BE INTERESTED IN

Kinetic mix at gas-shell interface in inverted corona fusion targets

View Online   Export Citation   CrossMark

W. M. Riedel,[1,a] N. B. Meezan,[2] D. P. Higginson,[2] M. Hohenberger,[2] and M. A. Cappelli[1]

AFFILIATIONS

[1]Stanford University, Stanford, California 94305, USA
[2]Lawrence Livermore National Laboratory, Livermore, California, 94550, USA

[a]Author to whom correspondence should be addressed: wriedel@stanford.edu

ABSTRACT

Gas-filled, laser-driven "inverted corona" fusion targets have attracted interest as a low-convergence neutron source and platform for study-ing kinetic physics. At the fill pressures under investigation, ejected particles from the shell can penetrate deeply into the gas before colliding, leading to significant mixing across the gas–shell interface. Here, we use kinetic-ion, fluid-electron hybrid particle-in-cell simulations to explore the nature of that mix. Simulations of the system demonstrate characteristics of a weakly collisional electrostatic shock, whereby a strong electric field accelerates shell ions into the rarefied gas and reflects upstream gas ions. This interpenetration is mediated by collisional processes: At higher initial gas pressure, fewer shell particles pass into the mix region and reach the hotspot. This effect is detectable through neutron yield scaling vs gas pressure. Predictions of neutron yield scaling show excellent agreement with experimental data recorded at the OMEGA laser facility, suggesting that 1D kinetic mechanisms are sufficient to capture the mix process.

Published under an exclusive license by AIP Publishing. https://doi.org/10.1063/5.0059763

I. INTRODUCTION

There has been an expanded effort over the last several years to investigate the impact of kinetic behavior in inertial confinement fusion (ICF) targets, including interpenetration,[1,2] species separation,[3,4] diffusive mixing,[5] tail-depletion,[6] and beam-beam fusion.[7] Though work to understand mix in ICF has historically focused on hydrodynamic mechanisms, such as Rayleigh-Taylor and Richtmeyer-Meshkov instabilities,[8–11] experiments and simulations on exploding pusher platforms have demonstrated that significant mix can occur in situations where hydrodynamic instabilities are weak.[12] Kinetic effects are also suspected to play a role in the evolution of near-vacuum hohl-raums (NVH), which allow for improved laser coupling but which deviate strongly from hydrodynamic simulations.[13]

Recently, "inverted corona" fusion targets have generated interest as a low-compression neutron source as well as a platform for investigating kinetic physics.[14,15] Inverted corona targets consist of a fuel layer lined along the interior surface of a hollow or gas-filled plastic hohlraum (see Fig. 1). The laser beams enter the hohlraum through one or more laser entrance holes, where they illuminate the interior surface. The first studies of inverted corona targets focused on vacuum targets,[16–18] but in this work, we study targets that include windows covering the laser entrance holes and a fill gas. In gas-filled targets, the ablated fuel layer generates an inward-propagating shock that compresses and heats the

fill gas, resulting in temperatures approaching 10 keV and significant neutron yield. A key practical advantage of inverted corona targets is their low symmetry requirements: They can even be driven by single-sided illumination without significant yield degradation.[14]

Inverted corona targets enable the study of the interaction between a laser-ablated shell with a low-density background gas. The degree of mix and interpenetration as the ablated plasma converges will alter the composition of the plasma at the stagnation point. In this work, we perform numerical simulations of these targets using a kinetic-ion, fluid-electron hybrid particle-in-cell approach to investigate the nature of mix and predict experimental results.

The remainder of this work is organized as follows: Sec. II provides a description of the one-dimensional (1D) hybrid simulations as well as the experimental configuration that motivates our computational studies. The evolution of the system and nature of the mix process are discussed in Sec. III. In Sec. IV, we compare the neutron yields predicted by the simulations to the results of recent experiments conducted at the OMEGA laser facility. The conclusions are presented in Sec. V.

II. SIMULATION DESCRIPTION

The inverted corona targets under present investigation are shown in Fig. 1, designed for testing at the OMEGA laser facility.[19] These are spherical targets with an inner radius of 895 μm and a shell
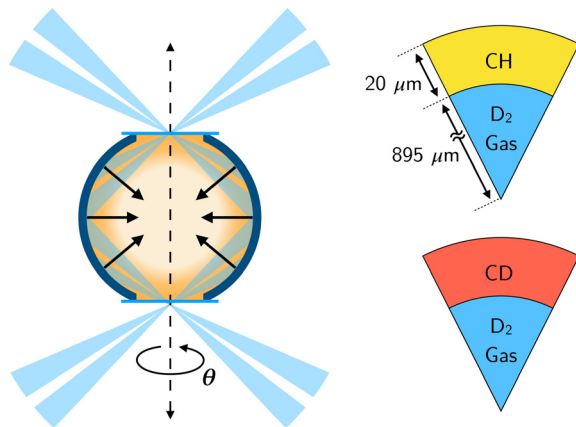
FIG. 1. Schematic of a cross section of an example gas-filled inverted corona target. Lasers pass through windows at the two poles to illuminate the interior surface of the shell. The resulting plasma stagnates at the target center.

thickness of 20 μm. The shells are either fully deuterated (CD) or non-deuterated (CH) plastic. In this case, the targets also include a D_2 fill-gas. The mass density is 1.1 g/cm^3, and the number ratio is 1:1 for both CD and CH shells. Real targets have one or two laser entrance holes covered by 1 μm thick transparent polyimide windows, but those are not included in 1D simulations. 18 kJ of laser energy is delivered by 40 laser beams in a 1 ns square pulse to the interior surface of the shell. Ejected plasma from the shell compresses and heats the fill gas, generating high-energy neutrons through the DD-n fusion reaction $D + D \rightarrow {}^3He + n$.

The extent to which ions comprising the shell extend into the fill gas is probed experimentally by running experiments with and without deuterated shells. During compression, some amount of shell material penetrates into the central hotspot before bang time, i.e., the time of peak neutron generation rate. If the shell is CD, then the D ions that mix in contribute to the neutron yield. H ions from CH shells do not react, and only yield from the initial fill gas will be produced. The difference in neutron yield between CH and CD targets at a given pressure, thus, provides a measure of how much shell material has reached the hotspot. Similar techniques to infer mix from fusion products are common in ICF.[5,12,20,21]

The system is simulated in 1D spherical symmetry using the particle-in-cell (PIC) code Chicago,[22–24] and compared against the multiphysics radiation hydrodynamics code HYDRA.[30] In Chicago, the ions are treated kinetically and the electrons as a massless fluid. The ions are treated kinetically and the electrons as a massless fluid. The plasma is assumed non-magnetized, and the electric field is described through a generalized Ohm's Law (see Ref. 7 for more information). Ion–ion collisions are modeled using the Nanbu method[25] modified for unequally weighted macro-particles.[26] Ion–electron collisions are modeled similarly to Ref. 27. Fusion reactions are modeled using a pairwise algorithm[28] that can handle arbitrary distributions of ion macroparticles. The plasma is assumed fully ionized at all times and is initialized at $T_e = T_i = 25$ eV. The choice of initial temperature may affect the evolution of the shock passing outward through the cold shell, but is expected to have a small effect on the inwardly propagating ablated plasma, which heats rapidly into the keV range and carries

most of its kinetic energy in its drift velocity. Radiation losses are expected to be small due to the relatively low-Z species present, so radiation is ignored in these simulations. Equivalent HYDRA simulations performed with and without radiation showed yield differences of only ~3%, and we perform an *a posteriori* estimate of this effect in the kinetic case in Sec. IV. An Eulerian computational grid with a cell width of 2 μm is used. The simulation domain extends from the origin to $r = 1025 \mu$m. Macroparticles that exit the domain are removed from the simulation.

Laser propagation is modeled in Chicago using a ray-tracing algorithm.[24] Laser macroparticles ($\lambda = 351$ nm) are injected inside the shell and absorbed through inverse bremsstrahlung.[29] The input laser intensity (which is absorbed with 100% efficiency) is scaled to match the absorbed power over time in equivalent 2D HYDRA[30] simulations (see Ref. 15 for more details). The maximum time step is limited by the Courant condition for the transit of photons across a cell (6.67 fs). The time step of the simulation is 6 fs, sufficient to resolve this timescale. The laser package and early plasma expansion of vacuum targets have previously been benchmarked against equivalent HYDRA simulations, showing good agreement.[15] The laser pulse is applied from $t = 0$ to $t = 1$ ns, and the system is evolved until $t = 3$ ns. Similar previous studies of exploding pusher targets[3,4] decoupled the laser, using profiles from hydrodynamic simulations at the end of the laser pulse as initial conditions for kinetic simulations. The integrated laser package in Chicago enables kinetic modeling from the start of the pulse.

It should be noted that the behavior of the deuterated and non-deuterated targets is not exactly hydro-equivalent due to the different atomic mass of D and H. However, this effect is small: The mass in the shell is dominated by C, and the overall evolution of the systems is comparable. Simulations of CH shells and artificially non-reacting CD shells show yield differences of less than 9% over the pressure ranges of interest. Figures in this work depict the evolution of a target with a CD shell, where the shell deuterium and gas deuterium are treated as separate species.

III. SYSTEM EVOLUTION

Contour plots of the number density of each species (gas D, shell D, shell C) in space and time are shown in Fig. 2 for 1 atm (a-c) and 6 atm (d-f) fill densities. At t = 0, the shell begins to absorb laser energy. The bulk of the shell is accelerated outward, but the plasma blowoff is ejected from the surface and expands toward the axis, compressing the gas until stagnation and rebound. Black contour lines indicate where most of the fusion yield is generated.

For comparison, two trajectories from equivalent HYDRA simulations are shown with dotted cyan curves. The inner cyan curve, which terminates at the target center, represents the position of the initial shock in HYDRA. The outer cyan curve, which converges and then slowly moves outward, represents the position of the gas-shell interface in HYDRA.

The initial density jump traveling through the gas is visible in the density plots (a) and (d) and roughly tracks the shock from HYDRA in both cases. This density jump reaches the axis at t = 0.68 ns for the 1 atm case and t = 0.84 ns for the 6 atm case. The electron temperature is nearly isothermal at $T_e \approx 2$ keV throughout the initial expansion, so the ion sound speed in the unperturbed plasma is estimated to be 310 km/s, and the Mach number of the initial density jump is roughly
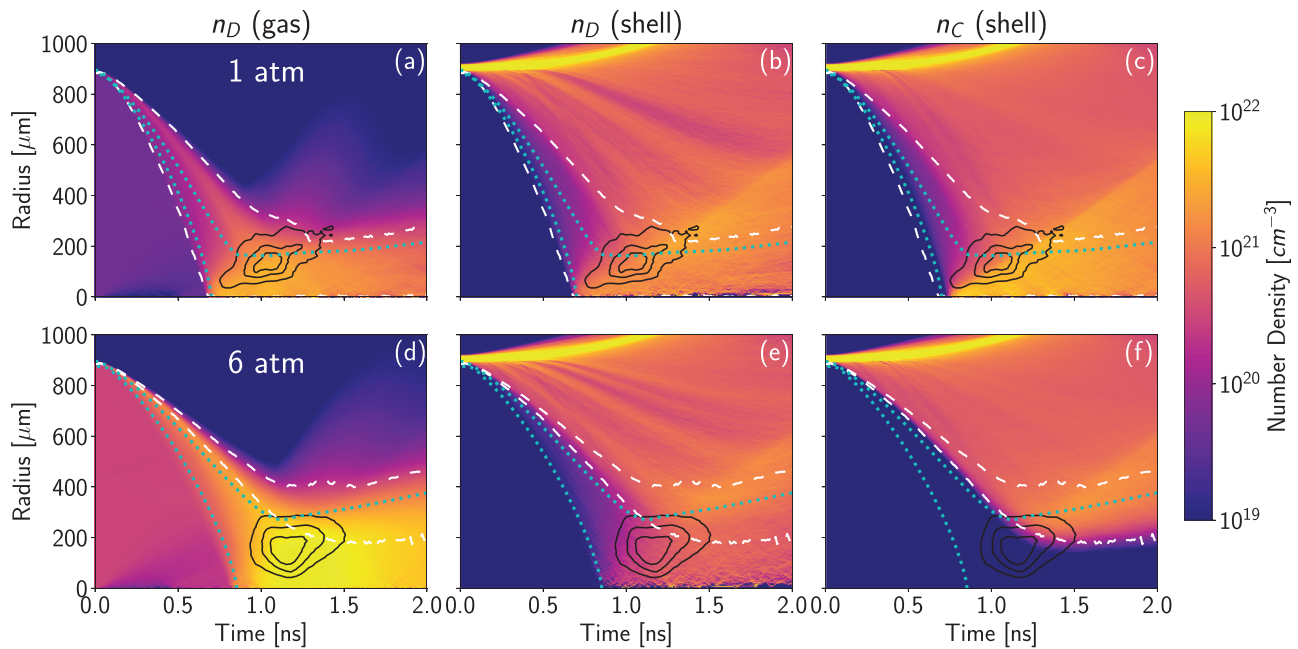
FIG. 2. Density contours for each species for two cases: 1 atm (a–c) and 6 atm (d–f). White dashed lines show the edges of the mix region. Cyan dotted curves show the position of the initial shock and the gas–shell interface in equivalent HYDRA simulations. At 1 atm, the mix region extends to the initial shock. At 6 atm, compression is slower and the growth of the mix region is reduced. Black contour lines show where fusion yield is generated. The levels represent 25%, 50%, and 75% of the peak fusion rate (neutrons/s/μm).

$M = v/\sqrt{Zk_B T_{e0}/m_i} = 4.25$ for the 1 atm case and $M = 3.44$ for the 6 atm case.

The two white dashed trajectories track the point in kinetic simulations at which the gas molar fraction $n_{Dgas}/(n_{Dgas} + n_{Dshell} + n_{Cshell})$ drops below 90% and 10%, defining the boundaries of the overlap region where both gas species and shell species are present. We shall refer to this area as the "mix region." The mix widths predicted here are larger than those of comparable exploding pusher targets.[3–5,12] This is partially due to reduced fill pressures and partially due to interior illumination: Laser energy is initially deposited directly at the gas–shell interface, and the plasma temperature increases rapidly as soon as the pulse begins. By contrast, for targets illuminated on the exterior surface, the interface remains cold until the complete ablation of the shell (burnthrough).

In the 1 atm case, the mix region extends all the way to the initial density jump and is more than 500 μm wide when it reaches the target center. In the 6 atm case, on the other hand, the mix region is narrower. It never reaches the axis and only approaches the edge of the hotspot ($r \approx 300$ μm) toward the end of yield production.

The expected mix width from diffusive processes can be roughly estimated using Fick's Law. In this case, the mix width $\Delta x = \sqrt{4D\tau}$, where D is the classical diffusion coefficient given by $D = (\langle Z \rangle + 1)k_B T/\langle m_i \rangle \nu$, $\langle Z \rangle$ is the average charge state, $\langle m_i \rangle$ is the average ion mass, ν is the ion–ion collision frequency, and τ is the diffusion time.[31] After 0.5 ns, the estimated mix width is 200 μm for the 1 atm case and 80 μm for the 6 atm case. These are of the same order as the widths observed in the simulations, although the diffusion estimate appears to underestimate the simulated width for the 1 atm case (300 μm) and overestimate the simulated width for the 6 atm case (32 μm).

Comparisons of number density, temperature, and velocity profiles for Chicago and HYDRA simulations of the 6 atm target at a single point in time (t = 0.5 ns) are shown in Fig. 3. Even at 6 atm, kinetic behavior is evident and the profiles do not match one-to-one, but a comparison is still informative. Different structure in the shocked gas is visible in Fig. 3(a), with a smoother shelf near the initial density jump in the kinetic case and more rapid compression of the outer edge of the gas in the hydrodynamic case. The critical electron density of the plasma is still far from the mix region in both cases and, in fact, eventually moves outward with the bulk slab shortly after shock breakout.

The ion temperature profiles [Fig. 3(b)] show slightly different structure near the edge of the cold shell, but the temperature of the shocked gas agrees reasonably well between hydrodynamic and kinetic simulations. The electron temperature is nearly isothermal in both cases, although it is lower in Chicago by around 25%, likely due to differences in the laser packages. Despite this difference, the velocity profiles [Fig. 3(c)] appear to match reasonably well, deviating only near the initial density jump, where fast ions are penetrating into the gas and the system has not strongly thermalized yet.

Phase-space plots of each species at the same point in time (t = 0.5 ns) are shown in Fig. 4 for both the 1 atm (a-c) and 6 atm (d-f) cases, illustrating that the mixing process is highly kinetic. The cold shell is visible on the right of each plot for the shell species. Ions have been ejected from that shell and are streaming inward toward the axis, passing through the gas without significantly thermalizing. In fact, the jets seem to roughly agree with the self-similar solution for plasma expansion into vacuum:[32] The density decreases exponentially and the velocity increases nearly linearly with distance from the critical density. The gas species at large radius has been
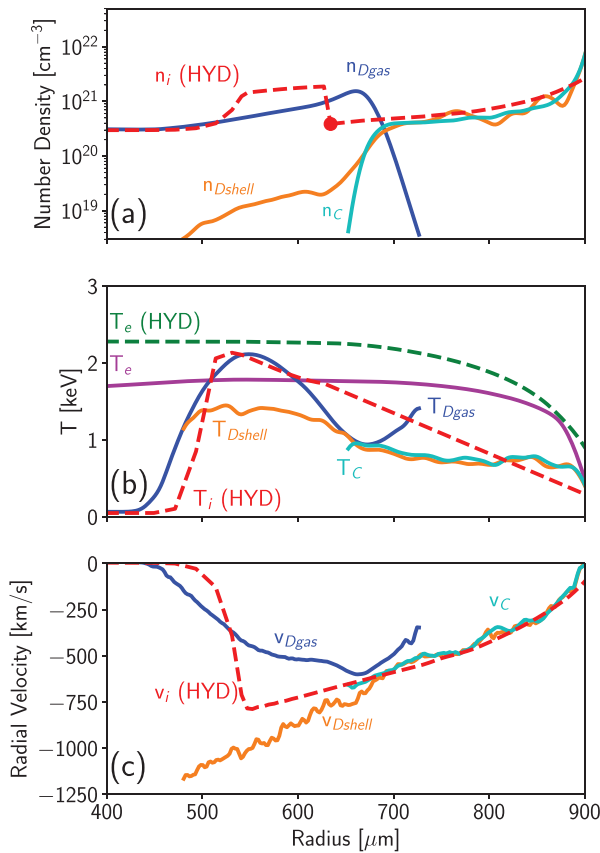
FIG. 3. Comparison of (a) number density, (b) temperature, and (c) radial velocity profiles of the plasma for the 6 atm target at t = 0.5 ns. HYDRA profiles are represented by dashed curves, and the red dot in (a) indicates the gas–shell interface. Note that in the single-fluid treatment of HYDRA, $n_i \equiv n_D = n_C$, $T_i \equiv T_D = T_C$, and $v_i \equiv v_D = v_C$ everywhere in the shell plasma. In the gas plasma, there is no C present. For $\lambda = 351$ nm, the critical electron density $n_c = 9.1 \times 10^{21}$/cc.

accelerated along with the jet and is counterstreaming back against the near-stationary gas at smaller radius. The two distinct populations of gas ions are visible in Fig. 4(a) between r = 350 and r = 500 μm. The tip of the jet marks the initial density jump propagating into the plasma, and the turning point of the gas species marks its outer edge.

The collisional mean free path for fast shell ions streaming into and slowing against a target plasma can be estimated by $\lambda_{mfp} = v_d/\nu_s$, where v_d is the shell ion drift velocity and the stopping frequency ν_s is given by[33]

$$\nu_s \approx 9 \times 10^{-8} \frac{n_{ip} A^{1/2} Z^2 Z_p^2}{\mu E_{ctr}^{3/2}} \ln \Lambda. \qquad (1)$$

Here, n_{ip} is the target number density, Z and Z_p are the streaming ion and target ion charge state, A is the mass number, μ is the reduced mass, and $E_{ctr} = A m_p v_d^2/(2 k_B)$ is the energy of the streaming ion. From this, the estimated mean free path of both C and D ions streaming into the 1 atm gas is greater than 300 μm. They are nearly free-

streaming across the mix region, and the mix width is limited by the position of the initial density jump in the gas. At 6 atm, on the other hand, the mean free path is estimated to be 90 μm for shell D ions and 30 μm for shell C ions. This pressure range roughly covers the range of weakly collisional systems, where the Knudsen number is of order unity. Estimated mean free paths agree reasonably well with the observed mix width (see Fig. 4), suggesting that collisions are mediating the growth of the mix region at higher pressure.

The non-Maxwellian behavior at the gas-shell interface bears resemblance to the formation of an electrostatic collisionless shock.[34] In an electrostatic shock, the shock is not formed through particle collisions, but instead through the bulk electric field generated by charge separation. The shock width can be much shorter than that of a collisional shock, which is typically on the order of the mean free path. Electrostatic shocks are often studied in the context of high-velocity counterstreaming flows that collide,[34–36] but can also be driven at the interface of two regions of plasma initially at rest.[36–39] They may be relevant to some aspects of ICF plasmas.[40,41]

In this case, there are two populations of plasma: the high-density shell and the low-density gas. In the simulation, they are initialized as fully ionized, but the temperature is low so they are essentially stationary. Starting at t = 0, laser energy is continuously deposited into the electrons near the critical density. The electron temperature quickly increases to the keV range. Electron thermal conduction is rapid due to their large thermal velocities, and so the electron temperature is nearly isothermal everywhere in the neighborhood of the critical density and throughout the low-density gas.

The electron temperature gradient is near zero across the interface, but the density difference at the interface leads to a large electron pressure gradient. Hot electrons from the high-density shell expand into the low-density gas, generating a strong ambipolar electric field that pulls the ions along with them. Charge neutrality is enforced in our simulations, so no actual charge separation occurs, but the acceleration due to the electric field is still captured and will be proportional to $(Z/A)\nabla P_e/n_e$,[24] where Z is the ion charge state, A is the mass number, and P_e and n_e are the electron pressure and number density. In this manner, thermal energy from the electrons is transferred into the directed kinetic energy of the ions.

The electric field acts on the plasma in the gas as well. Gas ions that begin near the interface will join the shell particles first ejected from the surface to form the front of the incoming jet. The tip of the jet represents the initial density jump in the gas. The inward expansion of these ions generates a broader pressure gradient that propagates along with the jet and accelerates all ions downstream of that density jump, bending the gas species distribution in phase-space and causing it to counterstream against itself. The edge of the gas would roughly correspond to the position of a collisionless shock: In this reference frame, the unperturbed gas is the upstream species, which flows toward the shock until it is reflected at the interface. The Mach numbers of this interface are $M = 2.3$ and 1.6 for the 1 atm and 6 atm case, respectively. These are somewhat higher than those observed in previous numerical studies, which could be due to additional compression from collisions.

A contour of the electric field in space and time is shown in Fig. 5 for both fill pressures. There is a strong electric field ~ 20 μm wide near the edge of the shell, and the broad pressure gradient is visible moving with the initial jump in density. During the initial expansion,
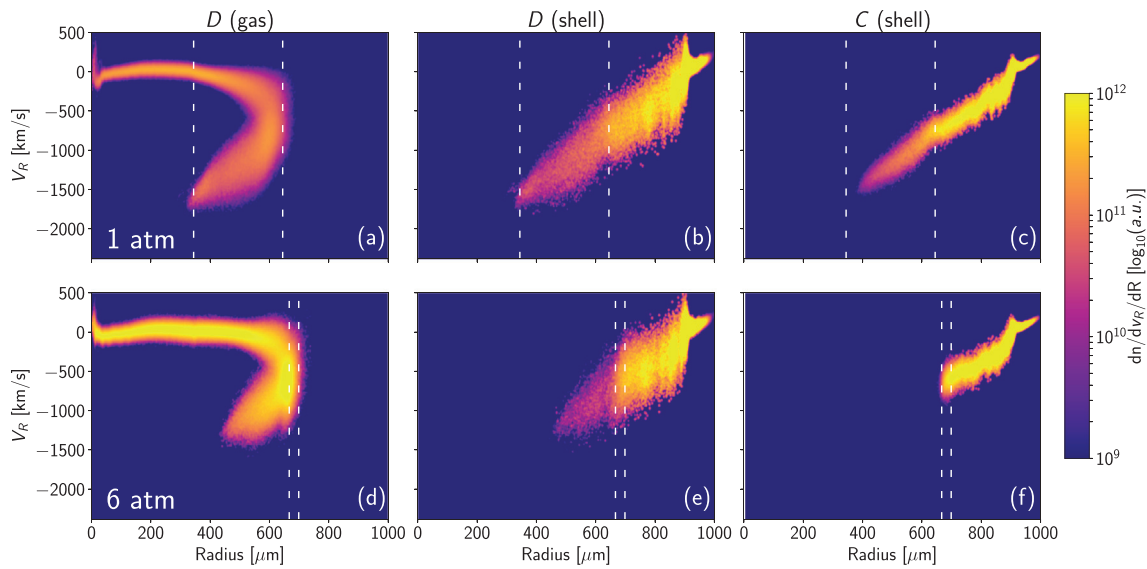
FIG. 4. Phase-space plots at t = 0.5 ns for each species for two cases: 1 atm (a–c) and 6 atm (d–f). The shell species penetrate into the gas, which is reflected and accelerated inward. In (a) between 350 and 500 μm, two distinct populations of gas ions with different mean velocities are visible. This effect is reduced at higher fill pressure. The mix region (indicated by the white dashed lines) is 300 μm wide for the 1 atm case and 32 μm wide for the 6 atm case.

the broad region of the electric field fluctuates around a roughly steady 2×10^7 V/m. For $E \propto \nabla P_e/q_e n_e$, a constant electric field with isothermal electrons corresponds to a density profile that decays exponentially in space, consistent with the self-similar vacuum solution in the underdense plasma.

A common characteristic of electrostatic shocks is a plateau downstream of the shock interface where ion acoustic oscillations are excited.[34] In the present case, this region is faint and no significant ion acoustic waves are observed. This is due to the large density ratio between the two initial regions, which has been shown to reduce the amplitude of these oscillations.[36] As the density ratio goes to infinity,

the solution should smoothly converge to the self-similar vacuum solution.

These simulations show that increasing the gas pressure causes both the initial density jump and the turning point interface of the gas to propagate more slowly and less shell material penetrates into the gas. This is a combination of two effects: the increased collisionality and the increased mass in the gas. Even ignoring collisions, targets at two different pressures are not hydro-equivalent. To isolate the effect of collisions, additional simulations were run in which the pressure was kept constant but the coulomb log was artificially scaled by a constant factor from its standard value.
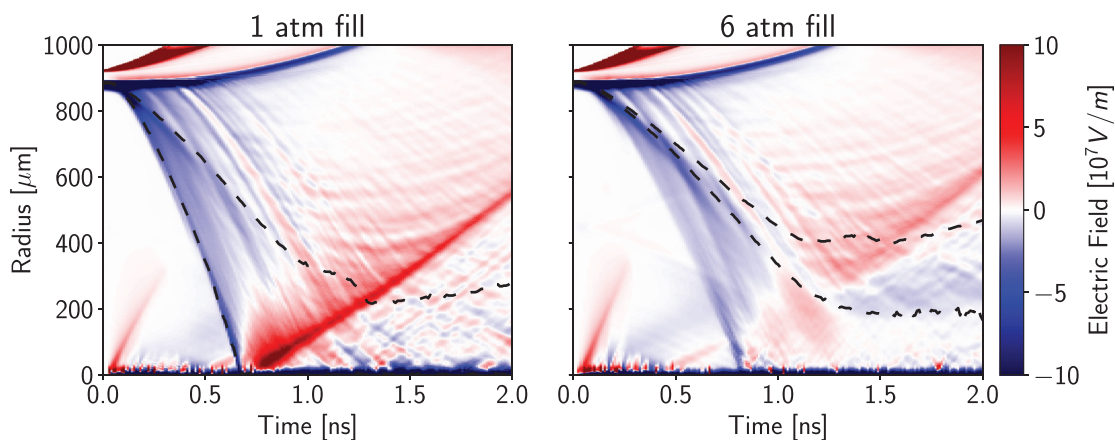

FIG. 5. Contours of the electric field in space and time. There is a spike in the field at the edge of the bulk shell, and a broad region of roughly constant field throughout the inwardly expanding plasma. The electric field begins to accelerate gas particles once they are passed by the initial jump in density. The broad field provides an acceleration of roughly 1000 (km/s)/ns. The black dashed curves depict the edges of the mix region.
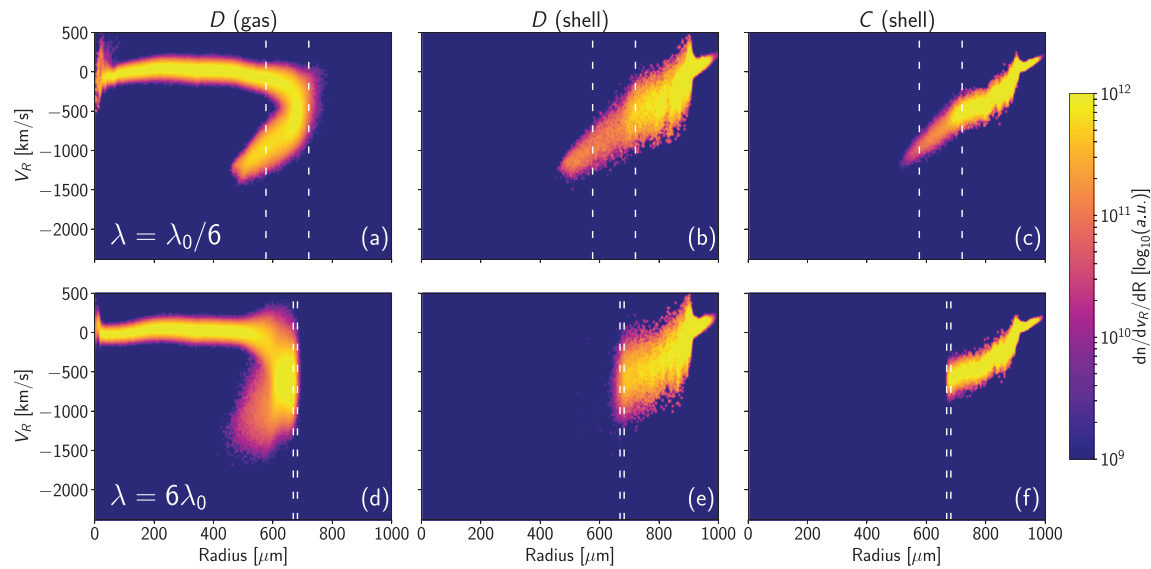
FIG. 6. Species phase-space plots for a 6 atm target at $t = 0.5$ ns with modified Coulomb logarithms: reduced by a factor of 6 in (a-c) and increased by a factor of 6 in (d-f). Rapid thermalization and a sharp gas–shell interface is visible for moderate increases in collisionality.

Phase-space diagrams of each species are shown in Fig. 6 for the less collisional (a–c) and more collisional (d–f) system at 6 atm at $t = 0.5$ ns. Compare these to the unmodified results in Figs. 4(d)–4(f). In the less collisional simulation [Figs. 6(a)–6(c)], the gas has been reflected without any significant thermalization, and both shell species are streaming through all the way to the front of the initial density jump. In the unmodified case [Figs. 4(d)–4(f)], the spread of the reflected gas distribution is wider (indicating increased heating) and the gas appears to be starting to thermalize at the interface. The lighter D species [Fig. 4(e)] is still able to penetrate $\sim 200\,\mu$m into the gas, but the more collisional C species [Fig. 4(f)] is stopped within $\sim 30\,\mu$m of the gas–shell interface. In the more collisional case [Figs. 6(d)–6(f)], a region of the shocked gas has clearly thermalized, and a sharp interface is formed at the edge of the gas region, through which neither shell species is able to penetrate.

Figure 7 shows how the boundaries of the mix region change with collisionality for the 1 atm case. The dotted lines represent the inner edge of the mix region, and the solid lines represent its outer edge for different levels of collisionality. The outer edge of the gas compresses more rapidly as collisionality increases due to the momentum imparted from shell particles stopped at the interface. As collisionality decreases the front of the mix region extends further inward, but only up to a point: Reducing the Coulomb logarithm below the unmodified case has no impact on its position. The front is ultimately limited by the velocity of the initial density jump in the gas. In the low-density limit, this can be estimated from the self-similar solution to expansion in vacuum, by finding the speed of the point where the density is equal to the initial gas density. Particles will not accelerate beyond this point, even in the absence of collisions: Once the density of the expanding jet falls below the density of the background gas, the electron pressure gradient (and, therefore, the electric field) goes to nearly zero. From Ref. 32, the velocity of this density contour is

$$v_g = c(1 - \ln(n_g/n_0)), \qquad (2)$$

where c is the sound speed of the shell, n_0 is the initial shell density, and n_g is the initial gas density. Assuming $T_e \approx 2$ keV, the estimated front speed is 1300 km/s for 1 atm and 1000 km/s for 6 atm.

The results of the modified simulations show that although there is significant counterstreaming and kinetic behavior present in these systems, the interaction is not truly a collisionless shock. Collisions mediate the behavior primarily by shrinking the mix region,
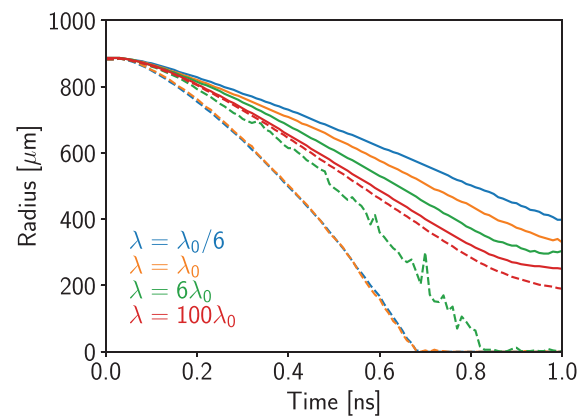

FIG. 7. Boundaries of the mix region for 1 atm at different modified Coulomb logarithms λ: $\lambda = \lambda_0/6$ (blue), $\lambda = \lambda_0$ (orange), $\lambda = 6\lambda_0$ (green), $\lambda = 100\lambda_0$ (red). Dashed lines represent 90% gas molar fraction, and solid lines represent 10% gas molar fraction. Higher collisionality compresses gas more rapidly, increasing the speed of its outer boundary. Reduced collisionality extends the front of the mix region inward, but the maximum speed is limited by the initial density jump passing through the gas, regardless of collisions. In this case, the front of the mix region has reached the initial density jump for both $\lambda = \lambda_0/6$ and $\lambda = \lambda_0$.

sharpening the gas–shell interface, and reducing the amount of material that is mixed in.

IV. YIELD VS FILL PRESSURE

Figure 8 plots neutron yield vs pressure for CH and CD targets, showing how mix is ultimately predicted to affect yield scaling. The green curves show yield prediction for equivalent HYDRA simulations of the targets. The HYDRA results represent the fully collisional, zero-mix expectations: Because no shell material penetrates into the gas, the majority of the yield depends only on the gas. As such, the scaling behavior of the CH and CD targets is similar. For the CD targets, the yield at 6 atm is 1.9 times above the yield at 1 atm. For the CH targets, this ratio is 2.5.

The blue curves show the yield predictions based on the present kinetic simulations. In this case, the CD and CH targets do not scale similarly with pressure. At low pressure, there is significant mix, and the yield of the CH target is reduced compared to that of the CD target by a factor of 5. As pressure increases, mix is reduced by the mechanisms described above, and the yields begin to converge. By 6 atm, the relative yields of the CH and CD targets are comparable to the results from the hydrodynamic case.

The absolute yields, however, are still somewhat lower than the fully collisional case. This gap is due to a combination of two factors. First, C ions mix into the hotspot and decrease the ion temperature. Even at 6 atm, the mix region does expand at later times, eventually extending into the edge of the hotspot [see Fig. 2(a) and 2(d)] and extinguishing some fusion events at the tail end of the implosion. As can be seen from the HYDRA trajectories of the gas–shell interface, the C ions do not penetrate as deeply in the hydrodynamic case. Second, some fast ions from the gas are able to escape the hotspot [see Fig. 2(a) and 2(d)]. These ions carry energy that would otherwise be converted into thermal energy, so the ion temperature is reduced.

It is possible that increased mix of C ions into the hotspot at lower pressures will lead to increased radiation loss, altering the yield scaling. Though radiation is ignored in these simulations, it is

worthwhile to estimate this effect. The approximate rate of bremsstrahlung energy emission can be calculated using Eq. (2.25) in Ref. 42. Given burn widths of ∼0.6 ns (∼0.55 ns) for the 1 atm (6 atm) case and hotspot conditions extracted from Chicago simulations, the total energy radiated during burn should be about 4% (0.2%) of the total hotspot energy density. If the ion temperatures are reduced by that fraction, the yield rate should be reduced by ∼10% (∼1%). Based on these estimates, the inclusion of radiation is likely to lead to slightly reduced yield for the low-pressure targets compared to that of the high-pressure targets, but should not dramatically affect the overall trends.

Increasing the collisionality changes the yield scaling to be more consistent with the hydrodynamic case, as expected. For CD targets, the yield ratio between the 6 atm and 1 atm cases is similar: $Y(6\,\text{atm})/Y(1\,\text{atm})$ is between 2 and 2.7 for all Chicago simulations. However, the CH yield scaling changes rapidly: $Y(6\,\text{atm})/Y(1\,\text{atm}) = 4.4$ for $\lambda = 6\lambda_0$, 8.7 for the unmodified case, and 17.0 for $\lambda = \lambda_0/6$. Additionally, the gaps in absolute yield compared to the hydrodynamic case are smaller for $\lambda = 6\lambda_0$.

For comparison, measured yields from inverted corona experiments conducted at the OMEGA laser facility are shown in red. 1D simulations overpredict the absolute yield, so all simulated values have been scaled down by a factor of 6.5 (matching experimental and simulated yields for CH targets at $P = 2$ atm) to allow easier comparison of relative values. After this correction, experimental data show excellent agreement with simulated predictions: The steeper slope of the pressure scaling for the CH target is reproduced, as is the relative yield between CD and CH targets at $P = 2$ atm.

These results confirm that there is significant mix occurring in these targets. Of course, 1D simulations cannot provide a complete description of the evolution of the system. There is evidence that multi-dimensional effects are weak (e.g., the low compression ratio and the fact that yield is insensitive to illumination symmetry), but we cannot rule them out with certainty. However, the experimental data gathered to this point suggest that 1D kinetic effects are at least sufficient to explain the observed yield behavior.

Previous higher-energy inverted corona experiments at the National Ignition Facility demonstrated larger yields than anticipated based on an expected scaling with laser energy.[14] These predictions were extrapolated from gas-filled targets with CH shells and ignored potential yield degradation from mix. After correcting for this degradation, the high energy shots are within a factor of two of predicted values. In general, when designing targets to maximize yield, reactions from ions in the shell must be considered in addition to the gas fill.

V. CONCLUSIONS

We have shown that capturing mix at the gas–shell interface is critical to modeling the behavior of inverted corona fusion targets. The mix region displays some characteristics resembling an electrostatic collisionless shock. Though the system is highly kinetic, the mix is mediated by collisional processes. Experiments with reactive and non-reactive shell species display measurable differences in the scaling of yield with fill pressure, and these comparisons can provide insight to how a laser-ablated shell expands and mixes into a low-density background gas.

In the future, it would be informative to perform follow-up experiments at higher and lower gas pressures to fill out Fig. 8 over a
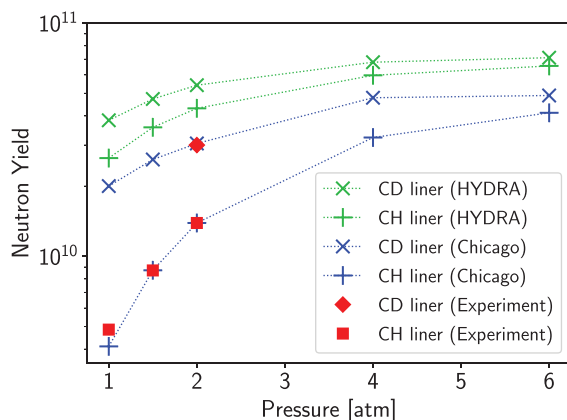

FIG. 8. Total yield vs gas fill pressure for CH and CD shells, for hydrodynamic simulation in HYDRA (green) and kinetic ion simulation in Chicago (blue). Also included are experimental data points (red). All simulated yields have been scaled down by a factor of 6.5 to match Chicago/experimental yields for CH target at $P = 2$ atm. Experimental data show excellent agreement with predicted pressure scaling and relative CD/CH yield.

wider range of mean free paths, especially for CD targets. Fill pressures in inverted corona targets are currently limited to ~3 atm or below due to fabrication constraints, but higher densities can be reached in cryogenically cooled targets (at the cost of increased complexity). In addition, experiments with separated reactants allow for the isolation of different categories of fusion events. Consider hydrodynamically equivalent targets of (1) a CH shell with a DD gas fill, and (2) a CD shell with ^{3}He gas fill. DD-neutron yield from (1) measures only fusion reactions between two gas ions. DD-neutron yield from (2) measures only fusion reactions between two shell ions. D^{3}He-proton yield from (2) measures fusion reactions between one ^{3}He ion in the gas and one D ion in the shell and is a direct measure of mix. Preliminary simulations suggest that these reactions peak at different times during the implosion and at different plasma conditions, so the fusion product spectra would provide further information on the temporal evolution of the system.

ACKNOWLEDGMENTS

AUTHOR DECLARATIONS
Conflict of Interest

The authors have no conflicts to disclose.

DATA AVAILABILITY

The data that support the findings of this study are available from the corresponding author upon reasonable request.

REFERENCES

[1]D. P. Higginson, P. Amendt, N. Meezan, W. Riedel, H. G. Rinderknecht, S. C. Wilks, and G. Zimmerman, "Hybrid particle-in-cell simulations of laser-driven plasma interpenetration, heating, and entrainment," Phys. Plasmas **26**, 112107 (2019).

[2]S. L. Pape, L. Divol, G. Huser, J. Katz, A. Kemp, J. S. Ross, R. Wallace, and S. Wilks, "Plasma collision in a gas atmosphere," Phys. Rev. Lett. **124**, 025003 (2020).

[3]A. Le, T. J. T. Kwan, M. J. Schmitt, H. W. Herrmann, and S. H. Batha, "Simulation and assessment of ion kinetic effects in a direct-drive capsule implosion experiment," Phys. Plasmas **23**, 102705 (2016).

[4]C. Bellei, H. Rinderknecht, A. Zylstra, M. Rosenberg, H. Sio, C. K. Li, R. Petrasso, S. C. Wilks, and P. A. Amendt, "Species separation and kinetic effects in collisional plasma shocks," Phys. Plasmas **21**, 056310 (2014).

[5]H. G. Rinderknecht, H. Sio, C. K. Li, N. Hoffman, A. B. Zylstra, M. J. Rosenberg, J. A. Frenje, M. Gatu Johnson, F. H. Séguin, R. D. Petrasso, R. Betti, V. Y. Glebov, D. D. Meyerhofer, T. C. Sangster, W. Seka, C. Stoeckl, G. Kagan, K. Molvig, C. Bellei, P. Amendt, O. Landen, J. R. Rygg, V. A. Smalyuk, S. Wilks, A. Greenwood, and A. Nikroo, "Kinetic mix mechanisms in shock-driven inertial confinement fusion implosions," Phys. Plasmas **21**, 056311 (2014).

[6]G. Kagan, D. Svyatskiy, H. G. Rinderknecht, M. J. Rosenberg, A. B. Zylstra, C.-K. Huang, and C. J. McDevitt, "Self-similar structure and experimental

[7]D. P. Higginson, J. S. Ross, D. D. Ryutov, F. Fiuza, S. C. Wilks, E. P. Hartouni, R. Hatarik, C. M. Huntington, J. Kilkenny, B. Lahmann, C. K. Li, A. Link, R. D. Petrasso, B. B. Pollock, B. A. Remington, H. G. Rinderknecht, Y. Sakawa, H. Sio, G. F. Swadling, S. Weber, A. B. Zylstra, and H.-S. Park, "Kinetic effects on neutron generation in moderately collisional interpenetrating plasma flows," Phys. Plasmas **26**, 012113 (2019).

[8]S. E. Bodner, "Rayleigh-Taylor instability and laser-pellet fusion," Phys. Rev. Lett. **33**, 761–764 (1974).

[9]M. J. deC Henshaw, G. J. Pert, and D. L. Youngs, "Non-linear Rayleigh-Taylor instability in (spherical) laser accelerated targets," Plasma Phys. Controlled Fusion **29**, 405–418 (1987).

[10]Y. Aglitskiy, A. L. Velikovich, M. Karasik, V. Serlin, C. J. Pawley, A. J. Schmitt, S. P. Obenschain, A. N. Mostovych, J. H. Gardner, and N. Metzler, "Direct observation of mass oscillations due to ablative Richtmyer-Meshkov instability in plastic targets," Phys. Rev. Lett. **87**, 265001 (2001).

[11]V. A. Smalyuk, S. X. Hu, J. D. Hager, J. A. Delettrez, D. D. Meyerhofer, T. C. Sangster, and D. Shvarts, "Rayleigh-Taylor growth measurements in the acceleration phase of spherical implosions on OMEGA," Phys. Rev. Lett. **103**, 105001 (2009).

[12]H. G. Rinderknecht, H. Sio, C. K. Li, A. B. Zylstra, M. J. Rosenberg, P. Amendt, J. Delettrez, C. Bellei, J. A. Frenje, M. Gatu Johnson, F. H. Séguin, R. D. Petrasso, R. Betti, V. Y. Glebov, D. D. Meyerhofer, T. C. Sangster, C. Stoeckl, O. Landen, V. A. Smalyuk, S. Wilks, A. Greenwood, and A. Nikroo, "First observations of nonhydrodynamic mix at the fuel-shell interface in shock-driven inertial confinement implosions," Phys. Rev. Lett. **112**, 135001 (2014).

[13]L. F. Berzak Hopkins, S. L. Pape, L. Divol, N. B. Meezan, A. J. Mackinnon, D. D. Ho, O. S. Jones, S. Khan, J. L. Milovich, J. S. Ross, P. Amendt, D. Casey, P. M. Celliers, A. Pak, J. L. Peterson, J. Ralph, and J. R. Rygg, "Near-vacuum hohlraums for driving fusion implosions with high density carbon ablators," Phys. Plasmas **22**, 056318 (2015).

[14]M. Hohenberger, N. B. Meezan, W. M. Riedel, N. Kabadi, C. J. Forrest, L. Aghaian, M. A. Cappelli, M. Farrell, S. H. Glenzer, B. Heeter, R. Heredia, O. L. Landen, A. J. Mackinnon, R. Petrasso, C. M. Shuldberg, F. Treffert, and W. W. Hsing, "Developing 'inverted-corona' fusion targets as high-fluence neutron sources," Rev. Sci. Instrum. **92**, 033544 (2021).

[15]W. Riedel, N. Meezan, D. Higginson, M. Hohenberger, J. Owen, and M. Cappelli, "Interpenetration and kinetic effects in converging, high-energy plasma jets," High Energy Density Phys. **37**, 100861 (2020).

[16]H. Daido, M. Yamanaka, K. Mima, K. Nishihara, S. Nakai, Y. Kitagawa, E. Miura, C. Yamanaka, and A. Hasegawa, "Neutron production from a shell–confined carbon–deuterium plasma by 1.06 μm laser irradiation," Appl. Phys. Lett. **51**, 2195–2196 (1987).

[17]A. V. Bessarab, V. A. Gaidash, V. T. Nasyrov, G. F. Punin, V. G. Rogachev, A. V. Senik, N. A. Suslov, G. V. Tachaev, V. I. Shemyakin, D. T. Parsons, G. V. Dolgoleva, N. V. Zhidkov, V. M. Ozgorodin, G. A. Kirillov, G. G. Kochemasov, A. V. Kunin, D. N. Litvin, and V. M. Murugov, "Results of first experiments with fusion targets at the iskra-5 high-power laser installation," Sov. Phys., JETP **75**(6), 970–973 (1992), available at https://inis.iaea.org/search/search.aspx?orig_q=RN:24071132.

[18]G. Ren, J. Yan, J. Liu, K. Lan, Y. H. Chen, W. Y. Huo, Z. Fan, X. Zhang, J. Zheng, Z. Chen, W. Jiang, L. Chen, Q. Tang, Z. Yuan, F. Wang, S. Jiang, Y. Ding, W. Zhang, and X. T. He, "Neutron generation by laser-driven spherically convergent plasma fusion," Phys. Rev. Lett. **118**, 165001 (2017).

[19]T. Boehly, D. Brown, R. Craxton, R. Keck, J. Knauer, J. Kelly, T. Kessler, S. Kumpan, S. Loucks, S. Letzring, F. Marshall, R. McCrory, S. Morse, W. Seka, J. Soures, and C. Verdon, "Initial performance results of the OMEGA laser system," Opt. Commun. **133**, 495–506 (1997).

[20]P. B. Radha, J. Delettrez, R. Epstein, V. Y. Glebov, R. Keck, R. L. McCrory, P. McKenty, D. D. Meyerhofer, F. Marshall, S. P. Regan, S. Roberts, T. C. Sangster, W. Seka, S. Skupsky, V. Smalyuk, C. Sorce, C. Stoeckl, J. Soures, R. P. J. Town, B. Yaakobi, J. Frenje, C. K. Li, R. Petrasso, F. Seguin, K. Fletcher, S. Padalino, C. Freeman, N. Izumi, R. Lerche, and T. W. Phillips, "Inference of mix in direct-drive implosions on omega," Phys. Plasmas **9**, 2208–2213 (2002).

[21]C. K. Li, F. H. Séguin, J. A. Frenje, S. Kurebayashi, R. D. Petrasso, D. D. Meyerhofer, J. M. Soures, J. A. Delettrez, V. Y. Glebov, P. B. Radha, S. P. Regan,

S. Roberts, T. C. Sangster, and C. Stoeckl, "Effects of fuel-shell mix upon direct-drive, spherical implosions on omega," Phys. Rev. Lett. **89**, 165002 (2002).

[22]C. Thoma, D. R. Welch, R. E. Clark, N. Bruner, J. J. MacFarlane, and I. E. Golovkin, "Two-fluid electromagnetic simulations of plasma-jet acceleration with detailed equation-of-state," Phys. Plasmas **18**, 103507 (2011).

[23]C. Thoma, D. R. Welch, and S. C. Hsu, "Particle-in-cell simulations of collisionless shock formation via head-on merging of two laboratory supersonic plasma jets," Phys. Plasmas **20**, 082128 (2013).

[24]C. Thoma, D. R. Welch, R. E. Clark, D. V. Rose, and I. E. Golovkin, "Hybrid-PIC modeling of laser-plasma interactions and hot electron generation in gold hohlraum walls," Phys. Plasmas **24**, 062707 (2017).

[25]K. Nanbu, "Theory of cumulative small-angle collisions in plasmas," Phys. Rev. E **55**, 4642 (1997).

[26]D. P. Higginson, I. Holod, and A. Link, "A corrected method for coulomb scattering in arbitrarily weighted particle-in-cell plasma simulations," J. Comp. Phys. **413**, 109450 (2020).

[27]M. E. Jones, D. S. Lemons, R. J. Mason, V. A. Thomas, and D. Winske, "A grid-based coulomb collision model for PIC codes," J. Comp. Phys. **123**, 169–181 (1996).

[28]D. P. Higginson, A. Link, and A. Schmidt, "A pairwise nuclear fusion algorithm for weighted particle-in-cell plasma simulations," J. Comput. Phys. **388**, 439–453 (2019).

[29]T. B. Kaiser, "Laser ray tracing and power deposition on an unstructured three-dimensional grid," Phys. Rev. E **61**, 895–905 (2000).

[30]M. M. Marinak, G. D. Kerbel, N. A. Gentile, O. Jones, D. Munro, S. Pollaine, T. R. Dittrich, and S. W. Haan, "Three-dimensional HYDRA simulations of national ignition facility targets," Phys. Plasmas **8**, 2275–2280 (2001).

[31]P. Amendt, C. Bellei, and S. Wilks, "Plasma adiabatic lapse rate," Phys. Rev. Lett. **109**, 075002 (2012).

[32]R. Fabbro, C. Max, and E. Fabre, "Planar laser–driven ablation: Effect of inhibited electron thermal conduction," Phys. Fluids **28**, 1463–1481 (1985).

[33]B. A. Trubnikov, "Particle interactions in a fully ionized plasma," in *Reviews of Plasma Physics* (Springer, 1970), Vol. 1, p.105; available at https://books.google. com/books?hl=en&lr=&id=FabaBwAAQBAJ&oi=fnd&pg=PA1&ots=ZBf4BWW194 &sig=3f1p-PnOn91VdchMqg2F4_1JZtM#v=onepage&q&f=false.

[34]D. W. Forslund and C. R. Shonk, "Formation and structure of electrostatic collisionless shocks," Phys. Rev. Lett. **25**, 1699–1702 (1970).

[35]T. N. Kato and H. Takabe, "Electrostatic and electromagnetic instabilities associated with electrostatic shocks: Two-dimensional particle-in-cell simulation," Phys. Plasmas **17**, 032114 (2010).

[36]F. Fiuza, A. Stockem, E. Boella, R. A. Fonseca, L. O. Silva, D. Haberberger, S. Tochitsky, W. B. Mori, and C. Joshi, "Ion acceleration from laser-driven electrostatic shocks," Phys. Plasmas **20**, 056304 (2013).

[37]G. Sorasio, M. Marti, R. Fonseca, and L. O. Silva, "Very high mach-number electrostatic shocks in collisionless plasmas," Phys. Rev. Lett. **96**, 045005 (2006).

[38]M. E. Dieckmann, G. Sarri, L. Romagnani, I. Kourakis, and M. Borghesi, "Simulation of a collisionless planar electrostatic shock in a proton–electron plasma with a strong initial thermal pressure change," Plasma Phys. Controlled Fusion **52**, 025001 (2010).

[39]G. Sarri, M. E. Dieckmann, I. Kourakis, and M. Borghesi, "Shock creation and particle acceleration driven by plasma expansion into a rarefied medium," Phys. Plasmas **17**, 082305 (2010).

[40]L. Q. Shan, H. B. Cai, W. S. Zhang, Q. Tang, F. Zhang, Z. F. Song, B. Bi, F. J. Ge, J. B. Chen, D. X. Liu, W. W. Wang, Z. H. Yang, W. Qi, C. Tian, Z. Q. Yuan, B. Zhang, L. Yang, J. L. Jiao, B. Cui, W. M. Zhou, L. F. Cao, C. T. Zhou, Y. Q. Gu, B. H. Zhang, S. P. Zhu, and X. T. He, "Experimental evidence of kinetic effects in indirect-drive inertial confinement fusion hohlraums," Phys. Rev. Lett. **120**, 195001 (2018).

[41]H. B. Cai, L. Q. Shan, Z. Q. Yuan, W. S. Zhang, W. W. Wang, C. Tian, F. Zhang, J. Teng, S. Q. Yang, Q. Tang, Z. F. Song, J. B. Chen, W. M. Zhou, Y. Q. Gu, B. H. Zhang, S. P. Zhu, and X. T. He, "Study of the kinetic effects in indirect-drive inertial confinement fusion hohlraums," High Energy Density Phys. **36**, 100756 (2020).

[42]S. Glasstone and R. Lovberg, U. S. A. E. C. O. of Technical Information, and U. A. E. Commission, *Controlled Thermonuclear Reactions: An Introduction to Theory and Experiment* (Van Nostrand, 1960).